inorganics

MDPI

Article

B-Doped ZnO Nanoparticles: Defect Chemistry, Tensile Strain, and Tunable Optical Response

Lütfi Arda [1], Merve Mine Seker Perez [2], Ersin Ozugurlu [3] and Ilke Tascioglu [4,*]

[1] Department of Mechatronic Engineering, Bahcesehir University, Besiktas, Istanbul 34353, Türkiye; lutfi.arda@bau.edu.tr
[2] Graduate School of Science and Engineering, Marmara University, Istanbul 34840, Türkiye; mervemineseker@gmail.com
[3] Department of Mathematics, Istanbul Technical University, Maslak, Istanbul 34469, Türkiye; ozugurlue@itu.edu.tr
[4] Faculty of Engineering and Natural Sciences, Istanbul Topkapi University, Uskudar, Istanbul 34662, Türkiye
* Correspondence: ilketascioglu@topkapi.edu.tr

Abstract

ZnO and ZnO:5%B nanoparticles produced by sol–gel synthesis exhibit a single-phase wurtzite structure. X-ray diffraction (XRD) investigation reveals crystallite sizes in the range of 32.37–39.63 nm and microstrain values on the order of (1.98–8.03) $\times 10^{-4}$, despite the Uniform Stress Deformation Model (USDM) indicating the presence of considerable tensile stress. Significant band-tail states are introduced via boron doping, resulting in Urbach energies ranging from 110 to 193 meV and a narrowed optical band gap of 3.216 eV. With a refractive index range of 2.05–2.71, the material exhibits tunable optical characteristics. Violet and blue emissions originating predominantly from zinc interstitials (Zn_i) and zinc vacancies (V_{Zn}) dominate the photoluminescence spectra, while oxygen interstitial-related contributions remain relatively weak. A high spin density is confirmed by electron spin resonance measurements, which reveal a strong defect-related signal at $g \approx 2.294$. The formation of Zn_i/V_{Zn} defect centers due to charge compensation and ionic size mismatch induced by B^{3+} substitution for Zn^{2+} significantly modifies the band-edge states and optical constants. These defect-engineered properties render the material promising for applications in ultraviolet (UV) photodetectors, transparent conducting oxides, and electron transport layers in organic photovoltaic devices.

Keywords: B-doped ZnO; nanoparticles; photoluminescence; defects; ESR; energy gap; refractive index

Academic Editor: Aivaras Kareiva

Received: 16 December 2025
Revised: 5 February 2026
Accepted: 6 February 2026
Published: 16 February 2026

1. Introduction

Zinc oxide (ZnO) is widely regarded as a model n-type semiconductor whose prominence in nanotechnology stems from its characteristic optoelectronic parameters, including a direct wide band gap of approximately 3.37 eV, a high exciton binding energy on the order of 60 meV, and a strong visible emission band centered near 495 nm with substantial spectral broadening [1–5].

ZnO nanoparticles have emerged as a highly adaptable material system for advanced electronic, photonic, and antibacterial technologies. Their high electron mobility exceeding 200 $cm^2/V{\cdot}s$, together with superior thermal conductivity, supports efficient charge transport even under demanding operating conditions. In addition, the intrinsic nonlinear resistance behavior and adjustable surface electronic states of ZnO enable its application in

high-sensitivity photodetectors, low-threshold light-emitting diodes, and radiation-tolerant sensing devices [6–8]. Importantly, ZnO's inherent radiation resistance supports uses in the nuclear and aerospace industries, and its compatibility with wet chemical etching enables atomic-scale precision in device production. ZnO is at the forefront of functional nanomaterials research due to its unique properties [2,9,10].

Due to its many benefits, including low processing temperatures, great stoichiometric control, high chemical homogeneity, and inherent scalability, the sol–gel approach is widely used to fabricate ZnO-based nanostructures. In particular, the ability to introduce dopant elements into the precursor solution chemistry in a controlled manner [9,11] facilitates the engineering of defect populations (V_O, V_{Zn}, O_i, Zn_i, etc.) and their associated optical–electronic properties [12]. However, while many studies focus on thin-film geometries, comprehensive investigations systematically correlating crystallite size, microstrain, specific surface area, and defect statistics with optical and magnetic responses within a unified data framework remain relatively limited for nanoparticles.

Boron (B) doping, due to its small ionic radius and +3 valence state, induces charge compensation and local strain fields in the ZnO lattice through substitutional/interstitial mechanisms [13–17]. This alters the relative abundances and energy levels of defects (zinc vacancies, oxygen vacancies, interstitial oxygen, and interstitial zinc (Zn_i)), thereby modifying band-edge transitions, the Urbach tail, the refractive index spectrum, and the photoluminescence (PL) emission map. In the literature, B-doped ZnO has mostly been reported for its enhanced conductivity and band gap modulation [18]. For instance, Atılgan and Özel [16] examined how the boron doping level influences the properties of ZnO thin films. They prepared B-doped ZnO films on glass substrates via spin coating, with boron concentrations ranging from 1% to 5%. Their analysis of electrical, optical, morphological, and structural properties revealed a strong dependence on B concentration.

In nanoparticles, quantifying the crystallographic stress/strain pair, correlating optical constants through multi-model approaches, and jointly interpreting PL/ESR data to reveal defect–optical–mechanical coupling have often remained secondary objectives.

This study aims to quantitatively elucidate the role of B doping by correlating the structural, mechanical, and optical responses of sol–gel synthesized $Zn_{1-x}B_xO$ (x = 0.0 and 0.05) nanoparticles within a unified framework. In this context, X-ray diffraction (XRD) data were analyzed using the Williamson–Hall approaches (UDM/USDM/UDEDM) in addition to the Debye–Scherrer equation to separate crystallite size, microstrain, and internal stress contributions, thereby distinguishing peak-broadening effects arising from grain-size reduction and strain. The obtained structural parameters were cross-validated with optical measurements derived from the band gap and absorption edge. Moreover, the refractive index and extinction coefficient were estimated spectrally using the Kubelka–Munk transformation and various dispersion models. For direct monitoring of the defect landscape, the PL spectra were resolved using Gaussian decomposition, and the possible transition schemes for band-edge emission and deep-level bands in the visible region were discussed, along with defect-center assignments. Electron Spin Resonance (ESR) signals offered evidence for the presence of paramagnetic centers, supporting the PL interpretations. Thus, it was shown that B-doping redistributes microstrain and internal stress and that mechanical reconfiguration is reflected, via defect statistics, in the optical edge and sub-band emissions.

2. Results and Discussion

2.1. Characterization of ZnO: 5%B Nanoparticle

The X-ray diffraction (XRD) patterns of ZnO and ZnO: 5%B and the Rietveld refinement plot of ZnO: 5%B are shown in Figures 1a and 1b, respectively. As shown in Figure 1a, the diffraction pattern is dominated by the (101) reflection, which is characteristic of the

hexagonal wurtzite ZnO crystal structure (JCPDS Card No. 36-1451). No additional diffraction peaks attributable to secondary phases such as B_2O_3, BO_3, or BO_4 were detected within the instrumental resolution. Moreover, a comprehensive investigation was carried out using Rietveld analysis, and the obtained results were compared with those derived from XRD. According to the Rietveld analysis results, no secondary phase formation was observed in ZnO: 5%B nanoparticles, as shown in Figure 1b; in other words, only the ZnO phase was detected.

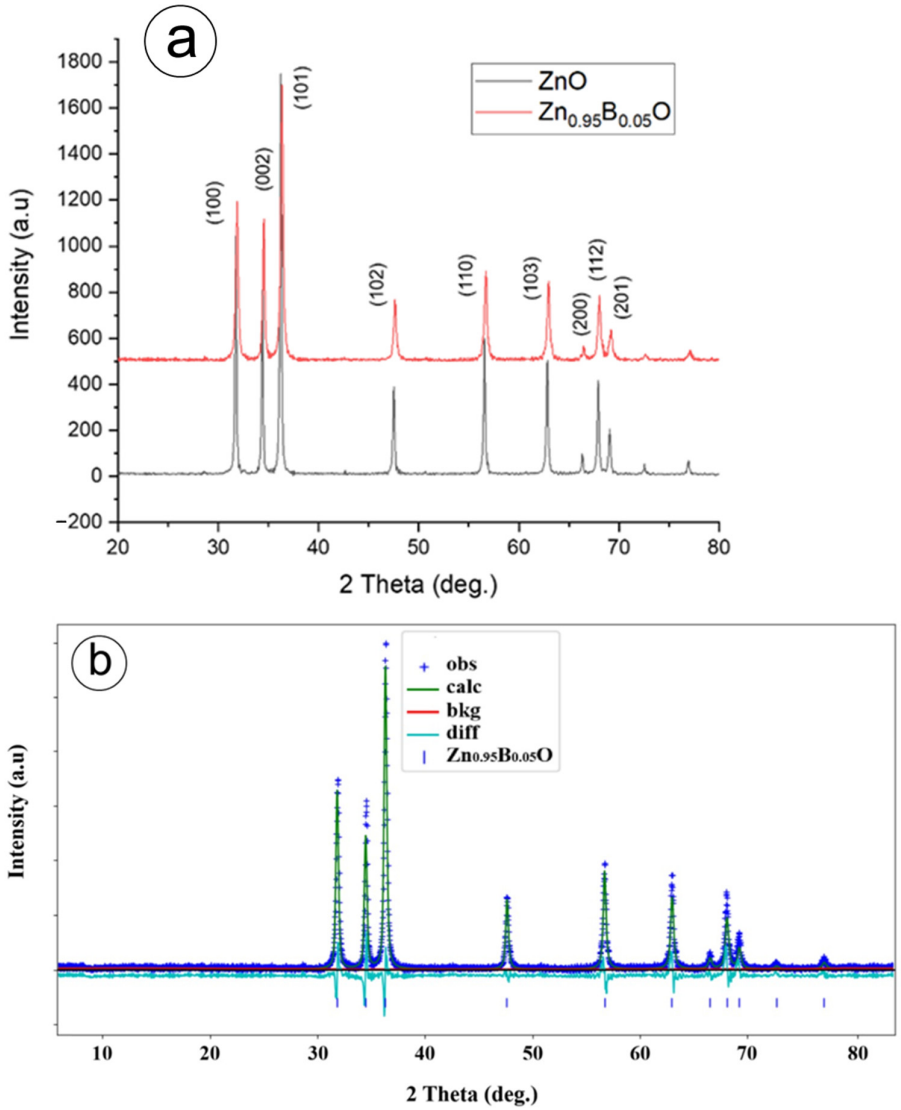

Figure 1. (**a**) The powder XRD patterns of ZnO and ZnO: 5%B nanoparticles synthesized by the sol–gel method. (**b**) Rietveld refinement plot of ZnO: 5%B (obs: observed, calc: calculated, bkg: background, diff: difference).

This absence of impurity-related reflections suggests that the incorporated B^{3+} ions are accommodated within the ZnO lattice, most likely through substitution at Zn^{2+} lattice sites.

It should be emphasized, however, that the absence of secondary crystalline reflections alone does not constitute direct proof of lattice-site occupancy, since amorphous boron–oxygen species or grain-boundary/adsorbed borate environments may remain undetectable by XRD.

However, the ionic radius of the Zn^{2+} ion in octahedral coordination is 0.74 Å, while the Shannon radius of the B^{3+} ion is approximately 0.23 Å. This indicates a significant radius mismatch ($\Delta r \approx 0.51$ Å), showing that the B^{3+} ion is considerably smaller than the Zn^{2+}

ion. This strengthens the conclusion that B doping will inevitably introduce substantial lattice strain and defect-mediated charge compensation.

Using the XRD data for ZnO and ZnO: 5%B nanoparticles, fundamental structural parameters such as bond length (L), dislocation density (δ), microstrain (ε), unit cell volume, lattice constants, and lattice distortion (σ) were calculated. The calculated values are presented in Table 1. The detailed equations used to calculate these parameters have been thoroughly explained in earlier studies [12,19–22].

Table 1. Lattice characteristics, average particle sizes, unit cell volume, c/a, dislocation density (δ) (the amount of defect in the sample), atom localization and displacement (u), and bond length (L) of ZnO and ZnO: 5%B nanoparticles.

Sample	D (nm)	a (Å)	c (Å)	c/a	Volume, V (Å^3)	$\delta \times 10^{-4}$ (nm^2)	u	L (Å)
ZnO	39.63	3.23	5.26	1.629	47.524	0.00064	0.376	1.9761
ZnO:5%B	32.37	3.239	5.189	1.602	47.144	0.00095	0.379	1.9712

Based on the data presented in Table 1, it is evident that 5% B doping induces a pronounced structural reorganization in the ZnO wurtzite crystal lattice. With 5% B incorporation, the average crystallite/particle size decreases from 39.63 nm to 32.37 nm, indicating that the dopant atoms suppress grain growth and promote enhanced nucleation. Examination of the lattice parameters reveals a slight increase in the a parameter (3.23 → 3.239 Å), while the c parameter exhibits a noticeable reduction (5.26 → 5.189 Å). As a result, the c/a ratio shifts to a lower value of 1.6020, deviating from the ideal wurtzite value (≈1.633). This behavior signifies an anisotropic lattice contraction predominantly along the c-axis, accompanied by the development of appreciable microstrain. Consistently, the unit cell volume decreases from 47.524 Å^3 to 47.144 Å^3, indicating an overall lattice densification. The increase in dislocation density from 0.00064×10^{-4} nm^{-2} to 0.00095×10^{-4} nm^{-2} further confirms that B doping enhances the defect density within the crystal structure. Moreover, the rise of the internal parameter u from 0.376 to 0.379 reflects a deviation from the ideal tetrahedral geometry of wurtzite ZnO, implying increased local bond asymmetry and charge separation. In contrast, the shortening of the Zn–O bond length from 1.9761 Å to 1.9712 Å is consistent with bond tightening and lattice distortion arising from the substitution of smaller B^{3+} ions at Zn^{2+} lattice sites.

Importantly, the observed anisotropic lattice evolution (c-axis contraction and reduced unit-cell volume), together with the correlated defect-related optical signatures discussed below, is consistent with boron incorporation that perturbs the ZnO host lattice. This interpretation is also consistent with prior studies in which XRD peak shifts and lattice contraction, supported by XPS identification of B^{3+}, were used to argue that boron dopants tend to occupy Zn lattice sites [20].

Overall, these results indicate that boron addition leads to a distinct structural modification in ZnO, characterized by grain refinement, anisotropic strain, increased defect density, and enhanced local polarization.

In ZnO: 5%B nanoparticles synthesized by the sol–gel method, it is necessary to carefully examine the stresses and strains to understand the defects formed due to B doping and the heat-treatment temperature. In the following, we assess stresses and strains in ZnO: 5% B nanoparticles using the Williamson–Hall (W–H) method [23] and compare the particle size with values obtained from Debye–Scherrer and W–H estimations.

2.2. Williamson-Hall (W-H) Analysis

The Debye–Scherrer equation was employed to compute the average crystallite size (Equation (1)) [24]:

$$D = \frac{K\lambda}{\beta_{hkl}\cos(\theta)} \quad (1)$$

where the full width at half maximum (FWHM) values of the three main diffraction peaks, (100), (002), and (101), were considered. D is the volume-weighted crystallite size, $K = 0.9$ for dimensionless form factor (0.9), λ for X-ray wavelength (0.1540 nm), β for line broadening in radians, and θ for Bragg angle in this expression.

Although the Debye–Scherrer formula can be employed to estimate the crystallite size, the lattice strain's contribution to peak broadening is not taken into consideration. Moreover, the observed line broadening is known to be caused by a combination of microstrain (ε) and finite crystallite size:

$$\varepsilon = \beta_{hkl}(4tan(\theta)) \quad (2)$$

According to Equations (1) and (2), these two parameters show distinct dependencies on the Bragg angle (θ), as seen by Stokes and Wilson [24].

To distinguish between these effects, the W-H analytical approach is employed. The fundamental idea is that tan(θ) is proportional to the strain-induced component of the integral breadth (β_{hkl}). In this work, different versions of the W-H technique were used to evaluate the lattice strain (ε), stress (σ), energy density (u), and crystallite size (D). These were the Uniform Deformation Energy Density Model (UDEDM) to determine ε, σ, u, and D; the Uniform Stress Deformation Model (USDM) to determine ε, σ, and D; and the Uniform Deformation Model (UDM) to determine ε and D.

2.2.1. The Model of Uniform Deformation

It is challenging to distinguish the distinct contributions of lattice strain and crystallite size to XRD peak broadening. To resolve this, the W-H technique proposes a mathematical model that incorporates both effects. Mote et al. [25] later refined this expression, leading to Equation (3):

$$\beta_{hkl}\ cos(\theta_{hkl}) = K\lambda/D + 4\ \varepsilon\ sin(\theta_{hkl}) \quad (3)$$

The UDM framework's W-H plots for ZnO and ZnO: 5%B are shown in Figures 2a and 2b, respectively, where the x-axis is represented by $4\varepsilon\ sin(\theta_{hkl})$ and the y-axis by $\beta_{hkl}\ cos(\theta_{hkl})$.

The data was fitted using a linear least-squares method with the formula $y(t) = A \times t + B$, where A is the slope of the graph of $\beta cos(\theta)$. The standard error sum of squares was minimized to identify parameters A and B:

$$E(A, B) = \sum_{i=1}^{N}[(B + At_i) - Y_i]^2 \quad (4)$$

The slope of the linear fit represents the lattice strain (ε) in this analysis, and the crystallite size (D) is calculated using the relation $D = K\lambda/y_{interception}$ from the y-intercept of the $\beta cos(\theta)$ axis. Table 2 provides a summary of the crystallite sizes, lattice strains, and stresses that were obtained for ZnO: 5%B nanoparticles using the UDM. Table 3a,b shows the relative errors for B concentration (using $N = 9$ reflection peaks) as well as the optimal parameters A (slope) and B (intercept) for the linear fits. Figures 2a and 2b display the appropriate Williamson-Hall plots ($\beta cos(\theta)$ versus $4sin(\theta)$), where the red lines indicate the linear fits for ZnO and ZnO: 5%B nanoparticles, respectively.

According to the values in Figure 2a,b, the fits show a positive slope. Section 2.3 presents a statistical analysis of these findings.

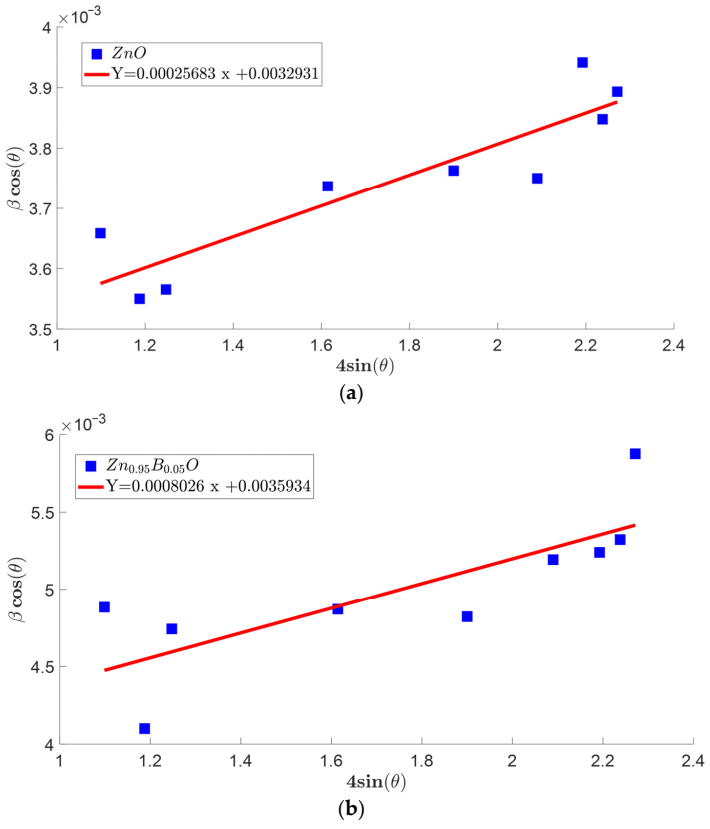

Figure 2. (**a**) The plot of $\beta cos(\theta)$ vs. $4sin(\theta)$ for ZnO. (**b**) The plot of $\beta cos(\theta)$ vs. $4sin(\theta)$ for ZnO:5%B.

Table 2. The crystallite size (D), lattice strain (ε), and strain (σ) values for all different methods, namely, the Debye–Scherrer, the UDM, USDM, and UDEDM, for ZnO and ZnO: 5%B structure.

	UDM		USDM				UDEDM					
Sample	**D (nm)**	**ε (10^{-4})**	**D (nm)**	**σ (N/m^2) (10^6)**	**ε_{max} (10^{-4})**	**ε_{avg} (10^{-4})**	**D (nm)**	**u (10^3)**	**σ_{max} (N/m^2) (10^6)**	**σ_{avg} (N/m^2) (10^6)**	**ε_{max} (10^{-4})**	**ε_{avg} (10^{-4})**
ZnO	42.09	2.57	41.52	0.029	1.98	2.29	41.82	0.0017	0.033	0.028	2.27	2.44
ZnO:5%B	38.57	8.03	38.24	0.097	6.72	7.77	38.51	0.0024	0.107	0.092	7.4	7.96

Table 3. (**a**) Coefficient of determination (R^2), adjusted coefficient of determination (R^2_{adj}), the root of the mean squared error (RMSE), and the total sum of squares (SST) for ZnO nanoparticle. (**b**) The linear fit: $y(t) = A \times t + B$ for ZnO nanoparticle.

(**a**)

Method	R^2	R^2_{adj}	**RMSE ($\times 10^{-5}$)**	**SST ($\times 10^{-7}$)**	**Correlation Coefficient**
UDM	0.819	0.793	6.2	1.5	0.905
USDM	0.802	0.774	6.5	1.5	0.896
UDEDM	0.816	0.789	6.3	0.2	0.903

(**b**)

Method	A	B	**Relative Error**	***p*-Value for *y*-Intercept**	***p*-Value for Slope**
UDM	2.56×10^{-3}	3.29×10^{-3}	2.70×10^{-8}	1.67×10^{-9}	7.9×10^{-4}
USDM	2.85×10^{-2}	3.33×10^{-3}	2.95×10^{-8}	1.12×10^{-9}	1.09×10^{-3}
UDEDM	1.92×10^{-3}	3.31×10^{-3}	2.75×10^{-8}	1.26×10^{-9}	8.45×10^{-4}

2.2.2. The Uniform Stress Deformation Model

All crystallographic directions are assumed to have isotropic strain under the UDM. This assumption, however, frequently does not apply to nanoparticles, where a more realistic analysis requires accounting for the anisotropy of the crystal's Young's modulus. The USDM and the UDEDM were developed to overcome this constraint [25].

Mote et al. [25] produced a modified equation in the USDM by substituting the anisotropic term σ/E_{hkl} for the isotropic lattice strain ε_{hkl} in the UDM, where E_{hkl} is the Young's modulus perpendicular to the set of crystal planes (hkl). The expression that results from this refinement is:

$$\beta_{hkl}cos(\theta_{hkl}) = K\lambda/D + 4\,\sigma/E_{hkl}\,sin(\theta_{hkl}) \tag{5}$$

The Young's modulus E_{hkl} for a hexagonal crystal structure is given by [26,27]:

$$E_{hkl} = \frac{\left[h^2 + \frac{(h+2k)^2}{3} + \left(\frac{a}{c}\right)\right]^2}{S_{11}\left[h^2 + \frac{(h+2k)^2}{3}\right]^2 + S_{11}\left[h^2 + \frac{(h+2k)^2}{3}\right]^2 + S_{33}\left(\frac{al}{c}\right)^4 + (2S_{13} + S_{44})\left[h^2 + \frac{(h+2k)^2}{3}\right]\left(\frac{al}{c}\right)^2} \tag{6}$$

and is a function of the elastic compliances $S_{ij}\left[m^2N^{-1}\right]$ where $S_{11} = 7.858 \times 10^{-12}$, $S_{13} = -2.206 \times 10^{-12}$, $S_{33} = 6.94 \times 10^{-12}$, $S_{44} = 23.57 \times 10^{-12} m^2N^{-1}$.

The USDM is represented by Equation (6), in which anisotropic strain results from the assumption that the stress is constant across all crystallographic orientations. The uniform stress σ is obtained from the slope of the linear fit in the appropriate W-H plot of $\beta cos(\theta)$ and $4sin(\theta)(1/E\_hkl)$, and the crystallite size D is obtained from the intercept on the $\beta cos(\theta)$ axis using the formula $D = K\lambda/y_{interception}$.

Figures 3a and 3b display the curves of $\beta cos(\theta)$ versus $4sin(\theta)(1/E\_hkl)$ (the USDM) for ZnO and ZnO:5%B, respectively; The USDM-estimated stress, lattice strain, and crystallite size are shown in Table 2. It was fitted using a linear least-squares method, $y(t) = A \times t + B$. In Section 2.2.1, the error function was provided using Equation (4). Tables 3b and 4b show the relative errors with the optimized A and B values, where $N = 9$ (the number of the reflection peaks) for ZnO and ZnO: 5%B nanoparticles, respectively.

Table 4. (**a**) Coefficient of determination (R^2), adjusted coefficient of determination (R^2_{adj}), the root of the mean squared error (RMSE), and the total sum of squares (SST) for ZnO:5%B. (**b**) The linear fit: $y(t) = A \times t + B$ for ZnO:5%B.

(**a**)					
Method	R^2	R^2_{adj}	**RMSE** ($\times 10^{-4}$)	**SST** ($\times 10^{-6}$)	**Correlation Coefficient**
UDM	0.627	0.574	3.2	1.9	0.792
USDM	0.724	0.684	2.7	1.9	0.851
UDEDM	0.682	0.637	2.9	1.9	0.826
(**b**)					
Method	A	B	**Relative Error**	***p*-Value for y-Intercept**	***p*-Value for Slope**
UDM	8.02×10^{-4}	3.59×10^{-3}	7.10×10^{-7}	6.39×10^{-5}	1.1×10^{-2}
USDM	9.68×10^{-2}	3.62×10^{-3}	5.25×10^{-7}	1.27×10^{-5}	3.63×10^{-3}
UDEDM	6.28×10^{-3}	3.59×10^{-3}	6.05×10^{-7}	2.85×10^{-5}	6.08×10^{-3}

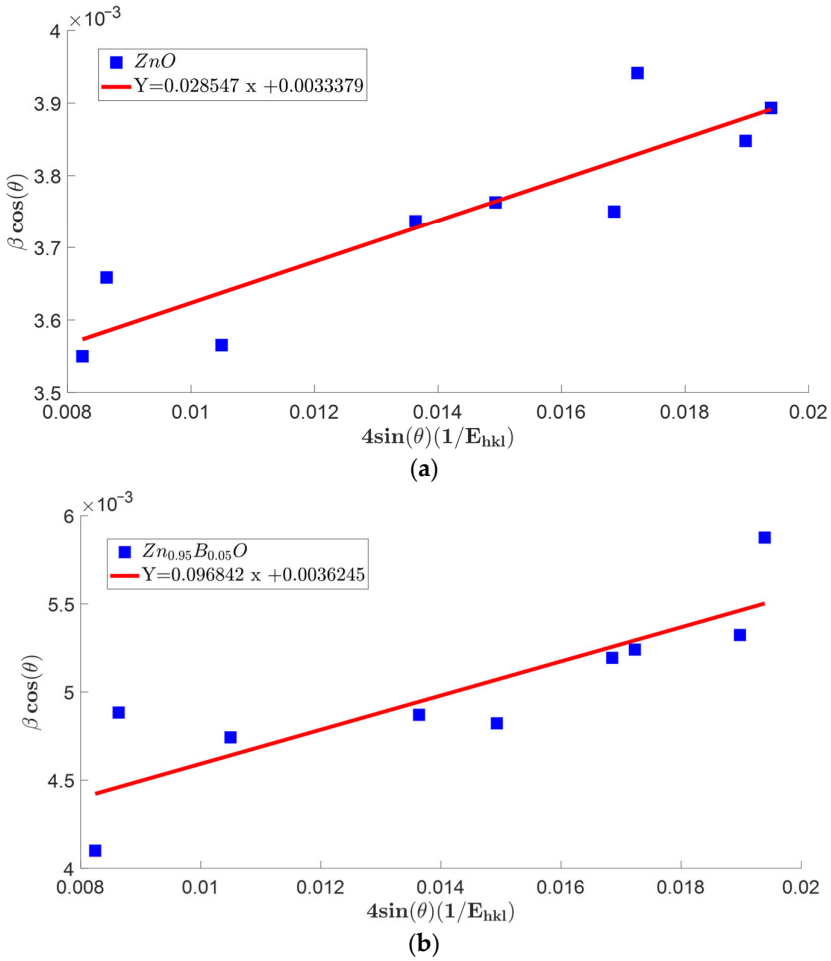

Figure 3. (**a**) The plot of $\beta cos(\theta)$ vs. $4sin(\theta)(1/E\_hkl)$ for ZnO. (**b**) The plot of $\beta cos(\theta)$ vs. $4sin(\theta)(1/E\_hkl)$ for ZnO:5%B.

2.2.3. The Energy Density Model of Uniform Deformation (UDEDM)

Mote et al. [25] developed the UDEDM, another W-H model, to determine the energy density u of a crystal. According to this method, anisotropic lattice strain originates from an isotropic deformation energy density. Equation (7) illustrates the relationship between strain ϵ and u for a homogeneous energy density:

$$u_{ed} = \frac{\varepsilon^2 E_{hkl}}{2} \tag{7}$$

based on Hook's law. Therefore, Mote et al. [25] improved Equation (5) to obtain Equation (1):

$$\beta_{hkl} cos(\theta_{hkl}) = \frac{K\lambda}{D} + 4\left(2\frac{u_{ed}}{E_{hkl}}\right)^{\frac{1}{2}} sin(\theta_{hkl}) \tag{8}$$

The UDEDM is represented by Equation (8). Applying a linear least-squares fit enables the slope of the line to estimate the energy density u when $\beta_{hkl} cos(\theta_{hkl})$ and $4\left(\frac{2}{E_{hkl}}\right)^{\frac{1}{2}} sin(\theta_{hkl})$ are given to the y-axis and x-axis, respectively. The intercept on the $\beta cos(\theta)$-axis provides the crystallite size D, or $D = K\lambda / y_{interception}$. The plots of $\beta cos(\theta)$ versus $4sin(\theta)\sqrt{(2/E_{hkl})}$ (the UDEDM) for ZnO and ZnO: 5%B are displayed in Figures 4a and 4b, respectively.

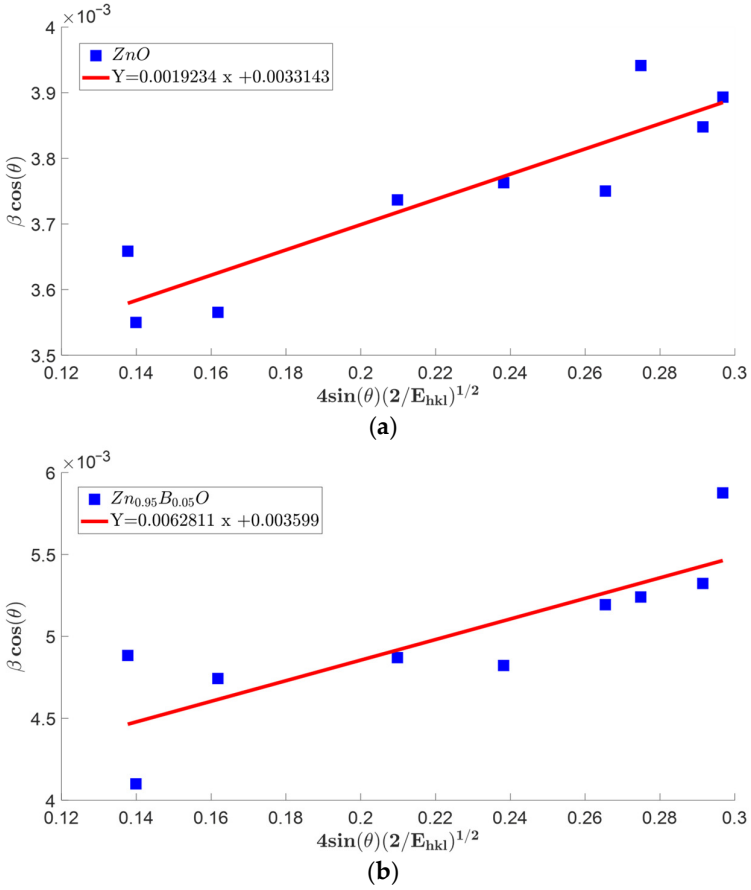

Figure 4. (**a**) The plot of $\beta cos(\theta)$ vs. $4sin(\theta)\sqrt{(2/E_{hkl})}$ for ZnO. (**b**) The plot of $\beta cos(\theta)$ vs. $4sin(\theta)\sqrt{(2/E_{hkl})}$ for ZnO:5%B.

Table 2 displays the estimated stress, crystallite size, and lattice strain as determined by the UDEDM.

It was fitted using a linear least-squares method, $y(t) = A \times t + B$. In Section 2.2.1, the error function was provided using Equation (4). Tables 3b and 4b show the relative errors with the optimized A and B values, where $N = 9$ (the number of the reflection peaks) for ZnO and ZnO: 5%B nanoparticles, respectively.

Among the Williamson–Hall approaches considered in this work, the uniform stress deformation model (USDM) yields results closest to those reported in previous studies [28]. Notably, the crystallite dimensions estimated using the USDM are in strong agreement with those obtained independently from TEM analysis, as shown in Table 1. The maximum stress and microstrain calculated via UDEDM for the nine peak planes (Figure 1) are presented in Table 2. Our observations indicate that the USDM is more suitable for nanoparticles than the UDEDM, which contradicts the conclusions of Mote et al. [25]. Table 2 presents a comparative overview of crystallite sizes derived using the Debye–Scherrer formula and UDM, USDM, and UDEDM.

The USDM shows that the average microstrain values for the nanoparticles are highly consistent, suggesting that the average microstrain affects both the energy density and the stress. These results are consistent with the findings of Mahendiran et al. [28]. Using the ICDD data file (Card No. 36-1451) for ZnO, which corresponds to the X-ray diffraction data for the nine planes, including their lattice characteristics and diffraction peaks, the phase identification was verified.

For ZnO and ZnO:5%B, the linear fits show a positive slope, as indicated in Figure 2b, which indicates positive uniform stress (σ) and, thus, tensile strain. Due to point defects in

the lattice, anisotropic microstrain is also indicated by the existence of this tensile strain. The crystallite size (D) for the ZnO: 5%B nanoparticle is compared across four distinct approaches: Debye–Scherrer, UDM, USDM, and UDEDM.

Section 2.3 provides a detailed discussion of the corresponding statistical data for the UDM, USDM, and UDEDMs.

Since the stress values are positive, it can be concluded that the structures undergo tensile stress. This also indicates the presence of anisotropic microstrain, likely due to point defects. Using the UDEDM method, average and maximum stress and microstrain values were obtained from the nine peak planes, as reported in Table 2. Notably, the crystallite size decreases with increasing dopant concentration.

2.3. Statistical Analysis

MATLAB's (R2020b) built-in function was used to evaluate the accuracy of the linear regression models; the relevant statistical metrics for the UDM, USDM, and UDEDMs are presented in Tables 3a and 4a. Even if the Total Sum of Squares (SST) and Root Mean Square Error (RMSE) values are roughly 10^{-8} and 10^{-4}, respectively, these metrics are not enough to verify the validity of the fits. From Tables 3a and 4a, it can be concluded that the linear model provides a good fit for the ZnO and ZnO:5%B samples, as their coefficients of determination (R^2) are bigger than 0.8. For pure ZnO, correlation coefficients above 0.8 indicate strong agreement compared to 0.65 in ZnO:5%B. However, relying solely on R^2 values and correlation coefficients can be misleading, as the F-statistic—which compares the linear regression model against a constant model—must also be considered. The *p*-value indicates the significance of the F-statistic.

The best results were obtained for pure ZnO, where the *p*-values for slopes were approximately 10^{-4}, 10^{-3}, and 10^{-4} for the UDM, USDM, and UDEDM methods, respectively, compared to 10^{-2}, 10^{-3}, and 10^{-3} for ZnO:5%B; and the *y*-intercept *p*-values were around 10^{-9} and 10^{-5}, as seen in Tables 3b and 4b. In other cases, the model either provides a good fit to the data or exhibits varying degrees of significance.

2.4. The Morphology of Nanoparticles

ZnO: 5%B nanoparticles were characterized using scanning electron microscopy (SEM) and transmission electron microscopy (TEM). Figure 5a presents the particle size distribution of ZnO:5% B nanoparticles at a magnification of 1 μm. The SEM micrograph clearly reveals compact, quasi-spherical, and agglomerated particle morphologies.

Figure 5c shows the particle size analysis of ZnO:5% B nanoparticles obtained using ImageJ software (version 1.54p) with Gaussian fitting. The average particle size was determined to be 30.61 nm. A slight discrepancy was observed between the average particle size obtained from ImageJ analysis (version 1.54p) and the values estimated directly from the XRD results, as summarized in Table 1.

Figure 5b illustrates the elemental composition of ZnO:5% B nanoparticles as determined by energy-dispersive X-ray spectroscopy (EDS). The observed EDS peaks and their relative intensity variations are consistent with the nominal precursor concentrations used during synthesis. The presence of only Zn, O, and B peaks, with no detectable signals from extraneous elements, confirms the intended doping composition of the synthesized samples.

Figure 6 displays TEM images of ZnO: 5% B nanoparticles at magnifications corresponding to 2 nm and 20 nm, respectively. The TEM image in Figure 6 shows that the nanoparticles tend to form agglomerates. TEM analysis further reveals that the sol–gel–synthesized ZnO:5% B nanoparticles exhibit well-defined ZnO crystalline features, in good agreement with the sharp XRD patterns shown in Figure 1. As observed in the inset of

Figure 6, the crystalline nature of the ZnO: 5%B nanoparticles is evident from the clear alignment of atomic planes across the micrograph, with an interplanar spacing of approximately 291 pm, which falls within the experimental range of 0.28 ± 0.01 nm. The d-spacing was estimated from the lattice-fringe pattern using FFT/line-profile analysis.

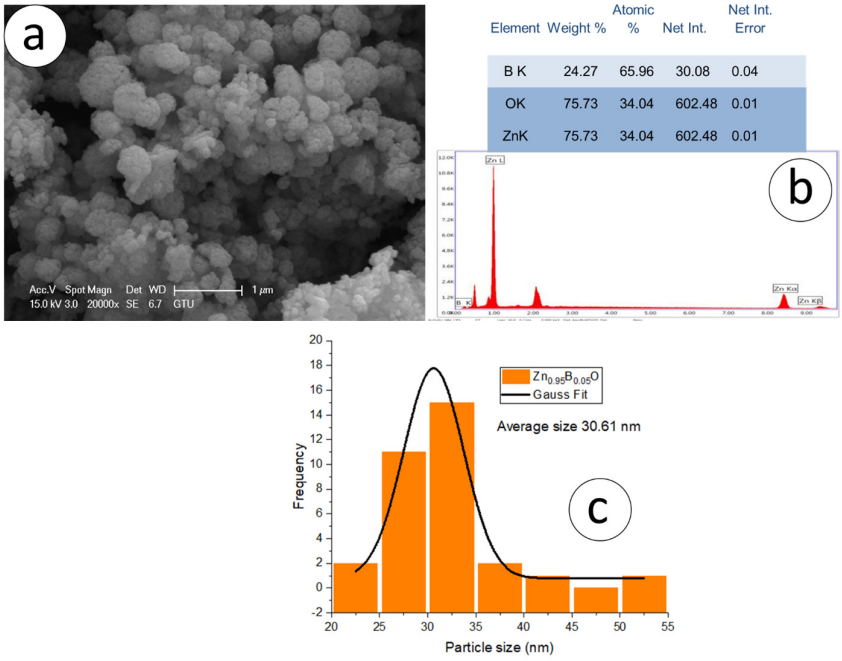

Figure 5. The SEM micrographs of ZnO: 5%B nanoparticles: (**a**) 1 µm, (**b**) EDS, and (**c**) the distribution of particle sizes ascertained via the Gaussian fitting.

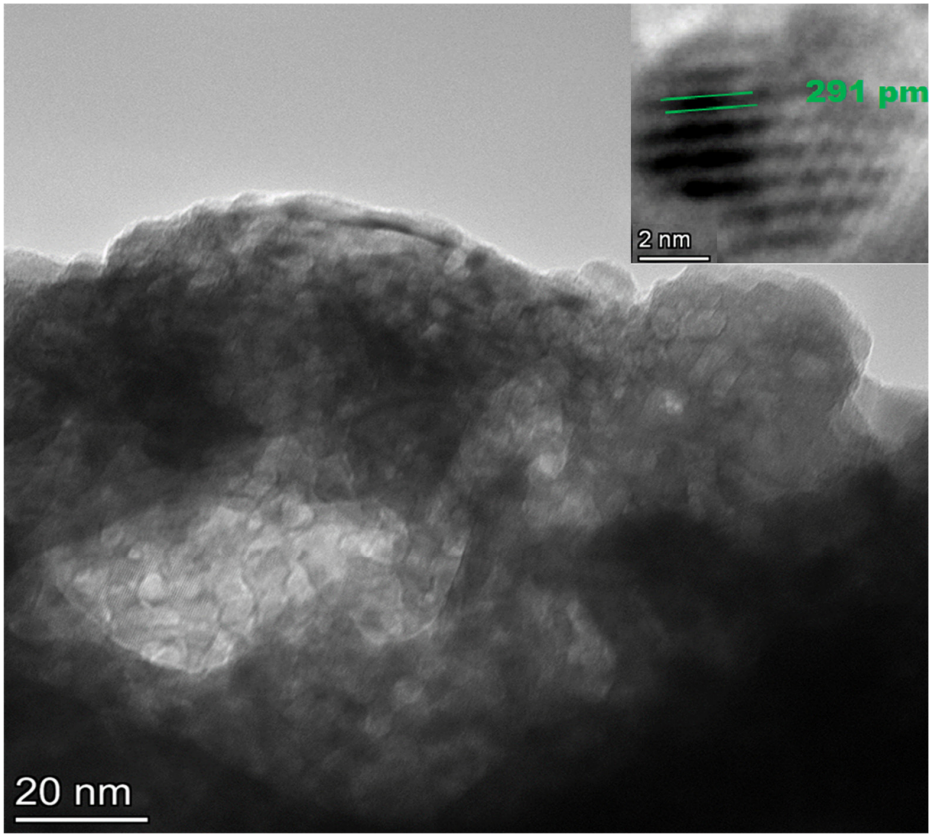

Figure 6. TEM image of ZnO:5%B nanoparticles; the inset reveals the crystallographic lattice planes ($d \approx 0.291$ nm).

When the lattice parameters $a = 3.239$ Å and $c = 5.189$ Å given in Table 1 for ZnO:5%B are used, the interplanar spacing of the (100) plane for the wurtzite hexagonal structure is calculated as:

$$d_{(100)} = \frac{\sqrt{3}}{2}a \approx 0.866a \quad (9)$$

In other words, $d_{(100)} \approx 0.866 \times 3.239,\ \text{Å} = 2.806$ nm.

By comparison with the experimentally obtained values, we confirmed that the interplanar spacing is (0.28 ± 0.01 nm); therefore, this value is consistent with the (100) crystallographic plane.

2.5. Optical Properties

2.5.1. UV-Vis Absorption Spectroscopy

The UV-Vis absorption spectrum of a sol–gel prepared sample of ZnO and ZnO: 5%B nanoparticles is shown in Figure 7.

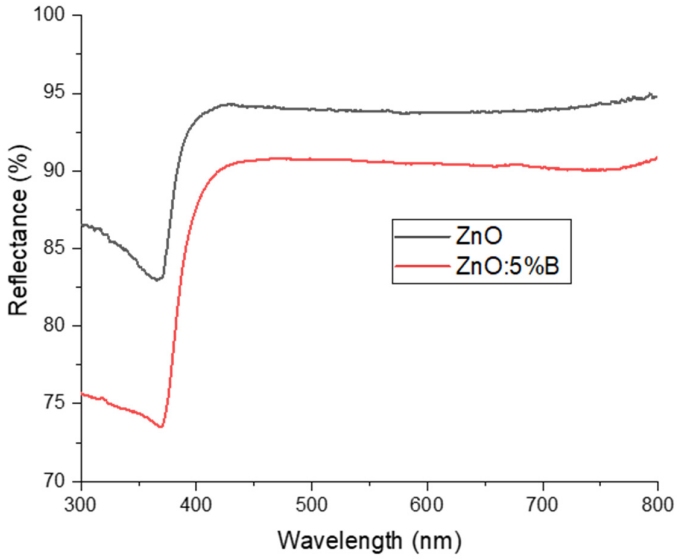

Figure 7. UV-VIS diffuse reflectance spectra of ZnO and ZnO: 5%B nanoparticle.

2.5.2. Band Gap Calculation

The diffuse reflectance $R_\infty(\lambda)$, obtained in relation to the ~100% reference ($BaSO_4$/PTFE), was translated into the Kubelka–Munk function because the absorption coefficient α could not be directly determined in ZnO and ZnO:5%B nanoparticles. A Tauc plot was created to find E_g, assuming $S(\lambda)$ approximately constant close to the edge and taking $F(R_\infty) \propto \alpha$.

$$F(R_\infty) = (1 - R_\infty)^2/(2R_\infty) = K/S \quad (10)$$

In this case, K stands for effective absorption, S for effective scattering, and R_∞ for reflectance in the 0–1 range. It is possible to write $F(R_\infty) \propto \alpha$ if it is assumed that S is weakly wavelength-dependent close to the absorption edge.

The optical band gap E_g can be computed using the following formula between the absorption coefficient (α) and the photon energy ($h\nu$):

$$\alpha h\nu = k\left(h\nu - E_g\right)^{\frac{1}{n}} \quad (11)$$

The optical band gap and energy-independent constants are denoted by E_g and k, respectively, in Equation (11). Since ZnO has direct permitted transitions and $F(R_\alpha)$ is proportional to α, n is assumed to be 1/2. Therefore, Equation (4) can be changed to:

Equation (11) uses the symbols E_g for the optical band gap and k for the energy-independent constants. Since $F(R_\alpha)$ is proportional to α, and ZnO has direct allowed transitions; n is taken to be 1/2. Consequently, Equation (10) can be modified to:

$$F(R_\alpha)h\upsilon = k\left(h\upsilon - E_g\right)^{\frac{1}{2}} \quad (12)$$

Stated differently, $(F(R_\alpha)h\upsilon)^2 = k^2\left(h\upsilon - E_g\right)$. The slope of the graph of $(F(R_\alpha)h\upsilon)^2$ vs. energy, shown in Figure 8, was estimated between 350 and 400 nm using a linear fit $y(h\upsilon) = A \times h\upsilon + B$ in the least-squares sense. Equation (13) provides the error formula for A and B, which was minimized to achieve this.

$$E(A,B) = \sum_{i=1}^{N}\left[A \times (h\upsilon)_i + B - \left((F(R_\alpha)h\upsilon)^2\right)_i\right]^2 \quad (13)$$

The parameters A and B, together with the corresponding relative error values, are summarized in Table 5, where $N = 9$ denotes the total number of data points.

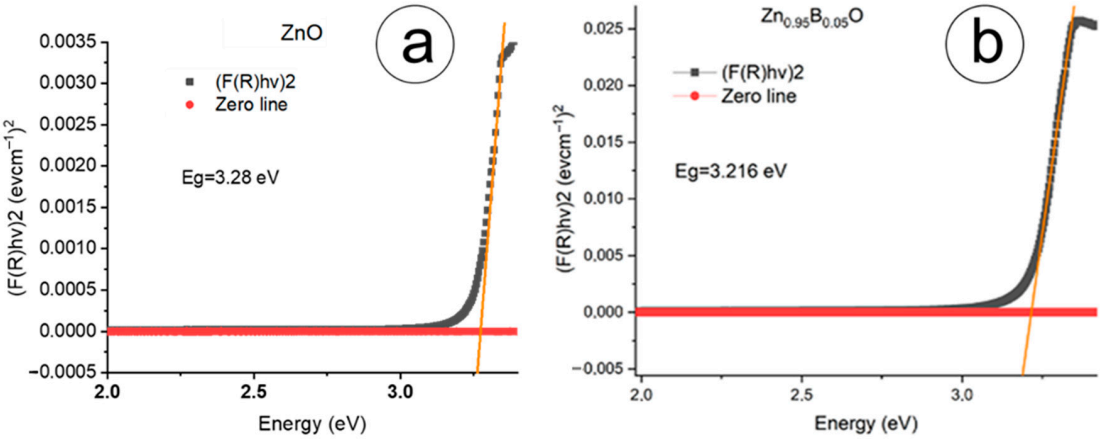

Figure 8. The linear fits for ZnO and ZnO: 5%B NPs, and the plot of $(F(R_\alpha)h\upsilon)^2$ as a function of photon energy $(h\upsilon)$. According to UV-Vis spectroscopy, the band gap energy for ZnO and ZnO: 5%B were (**a**) 3.28 and (**b**) 3.216 eV, respectively.

Table 5. Fitting curve function $(h\upsilon) = A \times h\upsilon + B$, band gap energy ($E_g$), and variance ($\sigma^2$) for ZnO and ZnO: 5%B nanoparticles.

A	B	E_g	σ^2
0.0554	−0.1819	3.28	7.87×10^{-9}
0.2023	−0.6506	3.216	2.16×10^{-6}

2.5.3. Refractive Index Calculations

In 2019, Naccarato et al. [11] showed how chemistry influences the band gap, the high refractive index connection, and why certain of the 4000 semiconductor material classes would perform better. They examined several models that used band gap measurements to determine the refractive index. These models include those of Ravindra et al. [29], Moss [30], Hervé and Vandamme [31], Reddy and Anjayenulu [32], and Kumar and Singh [33].

The refractive index values obtained in this study range from 2.09 to 2.71, as summarized in Table 6. These values represent effective refractive indices estimated from E_g-based empirical models, rather than wavelength-dependent dispersion data $n(\lambda)$. Accordingly, the refractive indices calculated using the models presented in Tables 6 and 7 are reliable. Based on the five models, Tripathy [34] reported the corresponding validity ranges for energy band-gap values in 2015, as listed in Table 8.

Table 6. Various techniques for calculating refractive indices (n) using band gap energy (E_g) for ZnO and ZnO: 5%B nanoparticles (effective refractive index values estimated from E_g-based empirical models; not wavelength-dependent dispersion $n(\lambda)$).

Sample	E_g	Moss [30]	Hervé and Vandamme [31]	Kumar and Singh [33]	Reddy and Anjayenulu [32]	Ravindra et al. [29]
ZnO	3.28	2.3199	2.2493	2.2957	2.6960	2.0504
ZnO:5%B	3.216	2.3313	2.2666	2.3104	2.7110	2.0901

Table 7. Refractive index formula based on the models.

Model	Refractive Index (n) Formula
Moss [30]	$\left(\frac{95}{E_g}\right)^{\frac{1}{4}}$
Hervé and Vandamme [31]	$\sqrt{1+\left(\frac{13.6}{E_g+3.47}\right)^2}$
Kumar and Singh [33]	$3.3668\ (E_g)^{-0.32234}$
Reddy and Anjayenulu [32]	$\left(\frac{154}{E_g-0.365}\right)^{\frac{1}{4}}$
Ravindra et al. [29]	$4.084 - 0.62\ E_g$

Table 8. Model-based reliability ranges for the energy band gaps.

Model	Confidence Intervals of Band Gaps
Hervé and Vandamme [31]	2.00 eV < E_g < 4.00 eV
Kumar and Singh [33]	2.00 eV < E_g < 4.00 eV
Reddy and Anjayenulu [32]	1.10 eV < E_g < 6.20 eV
Ravindra et al. [29]	1.50 eV < E_g < 3.50 eV
Moss [30]	0.17 eV < E_g < 3.68 eV

2.5.4. The Urbach Energy Calculation

According to the following connection, the absorption coefficient (α) at band boundaries has an exponential dependence on photon energy ($h\nu$), according to the Urbach law:

$$\alpha = \alpha_0 e^{h\nu/E_u} \tag{14}$$

where α_0 is a constant and E_u is the Urbach energy representing the impact of all potential faults [34]. The Urbach energy (E_u) is determined using the following relation:

$$E_u = \left[\frac{d(\ln(\alpha))}{d(h\nu)}\right]^{-1} \tag{15}$$

where α is the absorption coefficient and is the photon energy [35,36]. These values can be linked to the breadth of the localized states in the band gap. Figure 9 displays $\ln(\alpha)$ versus photon energy $h\nu$ (eV) of ZnO and ZnO: 5%B structure.

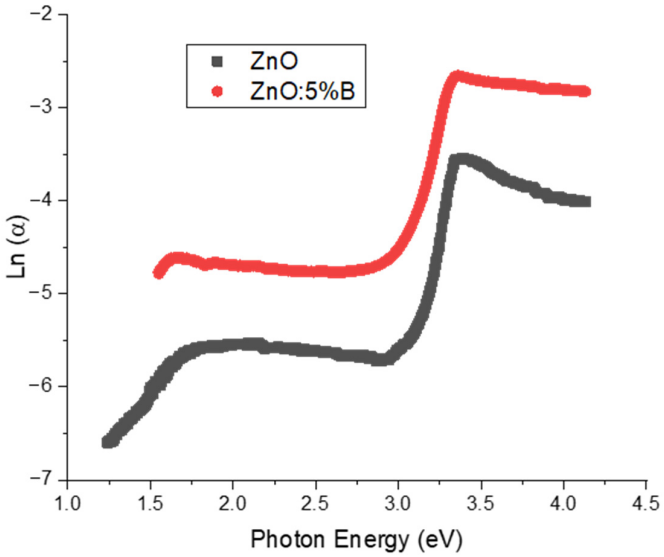

Figure 9. $\ln(\alpha)$ versus photon energy $h\nu$ (eV) of ZnO and ZnO: 5%B structure.

Owing to the discrete nature of the tabulated absorption coefficient data, the first derivative of $\ln(\alpha)$ with respect to photon energy ($h\nu$) was approximated numerically. For this purpose, three finite difference techniques (the 3-point backward, 3-point central, and 5-point formulas) were utilized. The associated approximation errors are of second and fourth order, respectively. The derived parameters for the ZnO:5%B structure are listed in Table 9.

Table 9. The Urbach energy values E_u in meV calculated at E_g by three different finite difference methods, namely, 3-point backward, central, and 5-point finite difference methods (FDM) of ZnO and ZnO: 5%B structure.

	3-Point Backward F.D.M. (meV)	3-Point Central F.D.M. (meV)	5-Point F.D.M. (meV)
ZnO	110.60	110.60	110.60
ZnO:5%B	192.35	184.85	191.53

Bindu and Thomas [37] reported an Urbach energy (E_u) of 490 meV for undoped ZnO nanoparticles. In contrast, the present results indicate that B incorporation at a concentration of 0.05 increases the Urbach energy. In this study, E_u is employed as a quantitative descriptor of local potential fluctuations and short-range structural disorder.

As listed in Table 9, the extracted E_u values lie in the range of approximately 184–193 meV. These values are evaluated in conjunction with the optical band gap (E_g), photoluminescence-derived defect populations (V_O and V_{Zn}), and key structural parameters, including micro-strain (ε), internal stress (σ), dislocation density (δ), internal positional parameter (u), and bond length (L). Overall, the increase in E_u indicates that B-induced disorder in ZnO nanoparticles broadens the band-tail states and can influence optical transition processes.

Despite the relatively moderate sensitivity of the refractive index models [30,31] to B-concentration, the growth in E_u may contribute to the slight variations in the $n(E_g)$ relationships that these models anticipate. The changes in E_g at the millielectronvolt (meV) scale have a small but noticeable impact on the refractive index (n). E_u, thus, may affect the refractive index (n) indirectly through disorder-induced band-edge modifications (via E_g), rather than serving as a direct controlling parameter.

E_u tends to rise as a result of the agglomeration and grain-boundary enrichment seen in SEM. Since the Urbach tail is particularly sensitive to short-range bond distortions and localizations originating from grain boundaries and interfaces, the relationship between E_u and XRD-derived Debye–Scherrer is not one-to-one. Instead, Debye–Scherrer provides information about long-range order within the crystal. Therefore, the observed increase in E_u upon B incorporation is more consistently interpreted as a signature of enhanced local disorder and band-tail broadening, rather than a simple monotonic function of crystallite size.

2.6. FTIR Studies

Fourier-transform infrared (FTIR) spectroscopy was employed to evaluate the chemical bonding structure and the possible incorporation site of boron in ZnO:5%B nanoparticles. The FTIR spectra of ZnO and ZnO:5%B nanoparticles are shown in Figure 10. As seen from the figure, this direct comparison reveals whether the bands in the 1451–1382 and 1028–1250 cm^{-1} regions are intrinsic to ZnO surface chemistry or are enhanced by boron incorporation.

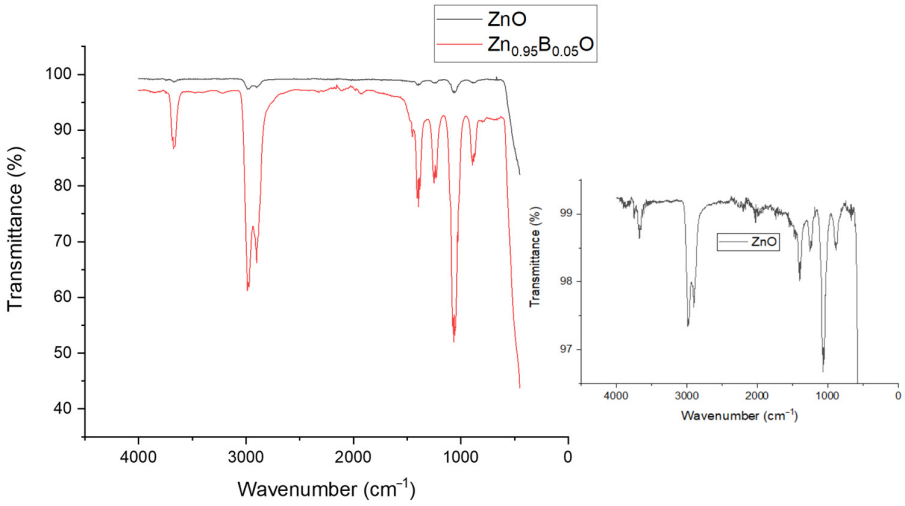

Figure 10. FTIR spectra of ZnO and ZnO:5%B nanoparticles. The inset shows a magnified view of the ZnO spectrum.

The broad absorption band observed in the 3200–3700 cm^{-1} region is attributed to O–H stretching vibrations of surface-adsorbed water molecules and/or hydroxyl (–OH) groups, which arise from the high specific surface area of ZnO nanoparticles. The pronounced band around ≈3675 cm^{-1} further supports this assignment. The weak bands observed at approximately ≈2988 and ≈2901 cm^{-1} can be associated with C–H stretching vibrations of trace residual organic species that may originate from the synthesis process.

In the mid-frequency region, the multiple-band structure observed in the 1451–1382 cm^{-1} range is commonly associated with carbonate (CO_3^{2-}) or C–O vibrational modes; however, it has also been reported in the literature that this region can partially overlap with boron–oxygen-based local environments (BO_3/BO_4 units) [38].

Notably, the corresponding spectral features in the 1451–1382 cm^{-1} region are also observed in undoped ZnO, supporting the view that this band group is predominantly related to carbonate/C–O surface species (e.g., atmospheric CO_2 adsorption), with possible partial overlap from borate-related local environments in the B-doped sample.

Nevertheless, the absence of a single broad and dominant absorption band characteristic of an amorphous boron oxide (B_2O_3) glassy structure indicates that significant boron oxide phase segregation is unlikely [39].

In particular, the bands observed in the 1028–1250 cm^{-1} range (1028, 1057, 1066, 1075, 1230, 1242, and 1250 cm^{-1}) can be considered consistent with boron–oxygen (B–O) vibrational modes and/or B–O–Zn linkages formed via oxygen within the ZnO lattice.

Compared to undoped ZnO, the band group in the 1028–1250 cm^{-1} region becomes more pronounced in ZnO:5%B, which strengthens its association with boron-related local bonding environments rather than solely generic ZnO surface vibrations.

The presence of these bands suggests that boron chemically interacts with the ZnO matrix and can be incorporated into the oxide network without forming a separate crystalline boron oxide phase. The enhancement of this band group in the FTIR spectrum indicates that the surface and/or local bonding environments of ZnO nanoparticles are modified by boron incorporation.

Such local changes in bonding chemistry, particularly due to the different charge state and ionic radius of B^{3+} compared to Zn^{2+} ions, can induce charge imbalance and local lattice distortions within the host lattice. This, in turn, increases the likelihood of forming intrinsic defects such as oxygen vacancies (V_O) and zinc vacancies (V_{Zn}). Indeed, the defect-related emission bands observed in the visible region of the photoluminescence (PL) spectrum are consistent with these structural and chemical modifications identified by FTIR, including the differences relative to undoped ZnO, indicating the activation of defect states.

Finally, the broad and intense absorption observed in the low-wavenumber region (<600 cm^{-1}) is a characteristic signature of Zn–O lattice vibrations, confirming that the ZnO host phase is preserved.

While the appearance and strengthening of the 1028–1250 cm^{-1} band group in ZnO:5%B supports boron-related local bonding environments (B–O and/or B–O–Zn linkages) and confirms chemical interaction of boron with the oxide network, FTIR alone cannot unambiguously distinguish substitutional lattice incorporation from borate species located at surfaces or grain boundaries. Therefore, the FTIR results are interpreted here as complementary evidence consistent with boron-induced local bonding modification, in agreement with the XRD/Rietveld lattice perturbation trends and the defect-related optical response discussed in the following sections.

2.7. Photoluminescence (PL)

PL measurements were performed at an excitation wavelength of 300 nm to probe defect-related states, defect concentrations, and crystalline quality in ZnO:5%B nanoparticles. As illustrated in Figure 11, the emission spectrum spans a broad wavelength range from approximately 3.54 to 1.46 eV (350 to 850 nm). The PL spectrum further reveals that the emission intensity of the ZnO:5%B nanoparticles reaches its overall maximum at around 3.18 eV (390 nm), corresponding to the near-band-edge (UV/violet) emission.

Consistent with our previous findings [12] and earlier reports in the literature, n-type ZnO semiconductors typically exhibit two distinct photoluminescence features: a broad visible emission band and a sharp ultraviolet (UV) emission peak. In ZnO-based nanostructures, the visible emission is commonly associated with intrinsic and extrinsic defect states; however, the UV emission serves as an indicator of both defect concentration and crystalline quality [19–21]. The UV emission originates from near-band-edge (NBE) recombination processes, primarily involving excitonic transitions between electrons in the conduction band and holes in the valence band. This near-band-edge emission is a hallmark optical property of ZnO, arising from its wide direct bandgap. A pronounced and narrow UV emission peak is generally indicative of high crystallinity and a low density of structural defects in ZnO nanoparticles. As evident from the UV emission spectrum

presented in Figure 11a, the ZnO:5% B nanoparticle sample exhibits a well-defined and sharp UV emission peak.

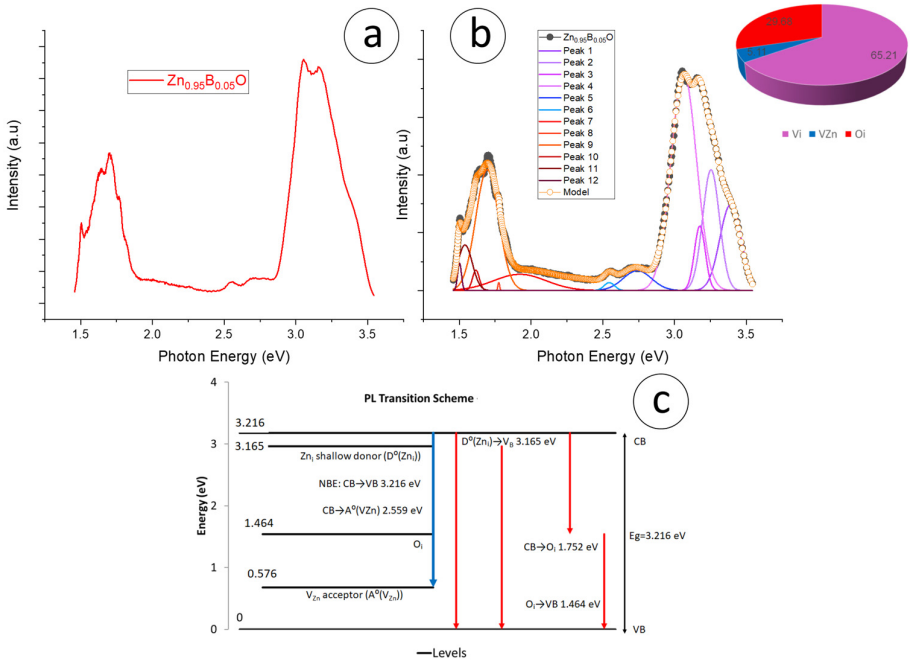

Figure 11. (**a**) PL spectra of ZnO: 5%B nanoparticle, (**b**) the PL spectra were Gaussian-deconvolved in photon-energy units (eV) after applying the $E = \frac{hc}{\lambda}$ conversion with the Jacobian intensity correction $I(E) = \frac{I(\lambda)\lambda^2}{hc}$ using the Fityk program (version 1.3.1); the inset pie chart shows the relative spectral weights (area fractions) of the resolved bands, and (**c**) PL transition scheme for ZnO: 5%B NPs.

Deep-level (DL) emission, commonly referred to as visible emission, is generally categorized into two broad spectral bands. The first emission band spans violet, blue, green, yellow, and orange wavelengths, while the second band extends into the red and near-infrared (NIR) regions. These emission features originate from radiative recombination processes involving various intrinsic defects and impurity-related states within the ZnO crystal lattice. Typical defect centers associated with these emissions include zinc interstitials (Zn_i), oxygen vacancies (V_o), oxygen antisites O_{Zn}, zinc vacancies (V_{Zn}), and oxygen interstitials (O_i), each contributing to characteristic emission energies.

It should be noted, however, that deep-level emission bands in ZnO are not uniquely assignable to a single defect species without complementary evidence (e.g., temperature/excitation dependence, time-resolved PL, or controlled-atmosphere annealing). Therefore, the following attributions are presented as literature-guided and non-unique.

$$f(\lambda) = ae^{-\frac{(\lambda-b)^2}{2c^2}} \quad (16)$$

To elucidate the defect states responsible for the emission features observed in Figure 11, the photoluminescence spectra were analyzed using the Gaussian peak deconvolution based on the model defined in Equation (16), implemented through the Fityk software package (version 1.3.1).

Although the experimental spectra are commonly presented in wavelength space, the quantitative analysis of the emission components was performed in photon-energy space (E, eV), since luminescence bands correspond to electronic transitions between discrete energy levels [40]. Accordingly, the wavelength-dependent intensity data were converted to energy units using $E = \frac{hc}{\lambda}$, and the appropriate Jacobian correction

$I(E) = \frac{I(\lambda)\lambda^2}{hc}$ was applied to account for the nonlinear $\lambda \leftrightarrow E$ transformation.

This conversion is necessary for physically meaningful Gaussian decomposition and for comparing peak positions/FWHM on an energy scale, as emphasized by Brik et al. [40] and commonly practiced in ZnO PL deconvolution studies reported in Uklein et al. [41] (e.g., ZnO band components expressed directly in eV).

The photoluminescence spectra of ZnBO nanoparticles that underwent Gaussian breakdown are shown in Figure 11b. There were twelve peaks in all, as the image illustrates. For compact reporting, these fitted sub-peaks were grouped into three conventional spectral regions (violet/blue/red) corresponding to the dominant visible-band contributions.

The following peaks represent emissions in the ultraviolet, violet, blue, red, and near-infrared (NIR) spectra: excitonic transitions occur between 3.27 and 3.26 eV (379 and 380 nm). Zinc interstitials (Zn_i) are the source of violet emissions 3.25–2.87 eV (382–432 nm) [17]. Zinc vacancies (V_{Zn}) are responsible for the blue emissions 2.67–2.54 eV (465–489 nm). Interstitial oxygen (O_i) is shown by red emissions 1.71–1.65 eV (727–750 nm). The weak emission observed in the red–NIR region (>750 nm) is attributed to deep-level defect states (e.g., oxygen interstitials or complex defect configurations), rather than to oxygen vacancies [19]. The PL spectra of ZnO:5% B nanoparticles generated by the sol–gel technique and decomposed using a Gaussian distribution in the Fityk software (version 1.3.1) are shown in Figure 11b. It was observed that defects such as Zn vacancies (V_{Zn}), zinc interstitials (Zn_i), and interstitial oxygen (O_i) were present. By calculating the area under each observed peak, the dominant emission contributions were determined. The results are shown in Table 10. Additionally, the relative spectral weights (area fractions) are summarized in Table 10. Here, "area under curve (%)" values are reported as relative spectral weights (area fractions) of the fitted emission components and should not be taken as rigorous defect concentrations. To address the $\lambda \leftrightarrow E$ nonlinearity, the spectrum was also evaluated in photon-energy space ($E = \frac{hc}{\lambda}$) using the appropriate Jacobian correction, and the dominant emission contributions were found to remain qualitatively consistent.

Table 10. The proportions of defects, emission ranges, emission sources, and peak locations using the Gaussian distribution were determined by analyzing the PL spectra of B-doped ZnO NPs using the Fityk software (version 1.3.1). (Reported "area under curve (%)" values represent relative spectral weights; qualitative indicator, not absolute defect concentration).

Area Under Curve (%)	Energy Range (eV)	Wavelength Range (nm)	Emission Range	Surface Defects	
65.21	2.75–3.26	380–450	Violet	$(Zn_i) \rightarrow (V_B)$	DL Emission
5.11	2.48–2.75	450–500	Blue	(v_{Zn})	
29.68	1.65–1.85	670–750	Red	(O_i)	

Fit robustness was checked by varying initial peak positions/FWHM and the background model within reasonable bounds; the main peak-energy regions and their relative dominance remained unchanged (qualitatively). Therefore, the reported area fractions are used only as relative spectral weights within this specific fit model and should not be interpreted as quantitative defect concentrations.

This distribution suggests (qualitatively) a defect chemistry dominated by Zn_i and V_{Zn} resulting from the charge surplus and size mismatch caused by the substitution of B^{3+} for Zn^{2+}. It is also consistent with the slight decrease in the band gap ($E_g = 3.216$ eV) and the broadening of the Urbach energy.

The substitution of B^{3+} ions for Zn^{2+} triggers compensation mechanisms in the lattice due to both charge imbalance (B^{+3} and Zn^{+2}) and size mismatch (B^{3+} being much smaller). As a result, point defects such as zinc vacancies (V_{Zn}, acceptors), zinc interstitials (Zn_i), and

oxygen interstitials (O_i) are primarily formed. This defect enrichment is consistent with the experimentally observed increase in microstrain (ε) and stress (σ), as well as with the broadening of the Urbach energy to the range of 110–193 meV and the slight narrowing of the band gap around E_g = 3.216 eV. In other words, the density of edge states has increased, the band edges have become blurred, and discrete/deep levels have significantly influenced the optical response. Therefore, this behavior is also consistent with the PL transition scheme (Figure 11c) and the paramagnetic centers observed in ESR signals.

2.8. Electron Spin Resonance

The ESR spectrum furnishes rich structural and electrical information, yielding critical insight into a material's magnetic centers. It is particularly effective for probing defect structures and magnetic behavior in nanomaterials by identifying sites associated with ion vacancies or localized magnetic ions [22].

The spin Hamiltonian (H), which quantitatively characterizes the magnetic interactions experienced by a magnetic center, is used to analyze the properties of the ESR spectrum [19,22]. The spin Hamiltonian's generic form is provided by:

$$H = \mu_B S g_e H + H_{cf} + SDS + SAI + \mu_N I g_n H + SJS + JS_1S_2 \quad (17)$$

The Zeeman effect, crystal-field splittings, and hyperfine couplings are some of the interactions that influence the spectral properties of electron spin resonance (ESR), such as line shape, position, and splitting. A detailed understanding of the local structure and magnetic environment of paramagnetic centers is made possible by analyzing these patterns. As a result, the ESR spectra of the B-doped ZnO nanoparticles were recorded in the first-derivative mode at ambient temperature. The experiments used 5 mW microwave power, 100 kHz field modulation, and a DC magnetic field applied perpendicular to the sample tubes and parallel to the microwave field. The ESR spectra are plotted as the derivative of absorption with respect to the external field (Figure 12).

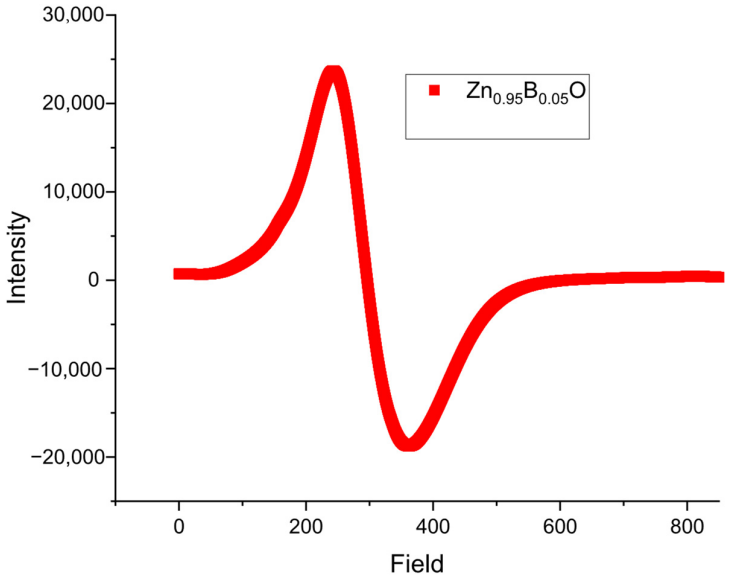

Figure 12. ESR spectra of all the samples ZnO: 5%B NPs.

The ESR spectra of ZnO: 5%B NPs in the 300–350 mT magnetic field range are shown in Figure 12. To guarantee accurate spectral representation, background signals from the empty quartz sample tube and the microwave cavity were removed before plotting. Within

the specified field range, a single, acute, and powerful resonance peak is consistently observed across all spectra.

As shown in Figure 12, ESR measurements were performed at room temperature (RT) to investigate the samples' defect characteristics. A large, single resonance peak was observed in the spectrum. Both the peak-to-peak line width (ΔH_{pp}) and the g factor were computed from the ESR data. For the ZnO: 5%B NPs annealed at RT, the ESR spectra and scaled experimental X-band ESR curves are shown in Figure 12.

The presence of structural flaws is responsible for the observed ESR peak intensity. The computed asymmetry factor (P_{asy}) values are shown in Table 11 and were obtained using the following formula according to Arda et al. and the reference therein [19]:

$$P_{asy} = 1 - h_u/h_L \tag{18}$$

where h_L and h_u correspond to the lower- and upper-side absorption peak heights relative to the baseline. Additionally, the following formula was used to determine the number of unpaired electron spins (N_s):

$$N_s = 0.285 \times I_{pp} \times \left(\Delta H_{pp}\right)^2 \tag{19}$$

where I_{pp} is the signal intensity from peak to peak, and ΔH_{pp} is the entire width at half maximum of the resonance peak [19].

Table 11. The ESR parameters for ZnO: 5%B NPs.

I_{pp}	ΔH_{pp}	P_u	P_l	P_{asy}	N_s	g-Values
4564.1	120.68	23,553.64	−18,989.54	2.24	14,289.52	2.294

The g-factor and the peak-to-peak linewidth ΔH_{pp} were assessed to obtain a better understanding of the spin relaxation mechanisms seen in the ESR spectra. The resonance condition was used to calculate the g-factor:

$$h\nu = g\mu_\beta H \tag{20}$$

where μ_β is the Bohr magnet, H is the resonance magnetic field, ν is the operating frequency of the X-band ESR spectrometer (9.45 GHz), and h is Planck's constant. When this equation is solved for g, the result is:

$$g = 71.4477\frac{\nu}{H} \tag{21}$$

As seen in Figure 13, the g-factor was calculated and plotted using Equation (21).

Room-temperature X-band ESR spectra of ZnO: 5%B nanoparticles exhibit a single, intense resonance line within 300–350 mT, characterized by $g = 2.294$, a peak-to-peak linewidth $\Delta H_{pp} = 120.7$ mT, and an asymmetry factor $P_{asy} = 2.24$. The single dominant line indicates a dominant ESR-active paramagnetic response (i.e., a prevailing resonance feature within the measured field window), rather than a uniquely identifiable single defect species, while the relatively high g-value (2.294) together with the broad linewidth points to defect-localized spins (vacancy/interstitial related), substantial defect density, and enhanced spin–spin interactions within a strained/disordered lattice environment.

Because g-values and broad linewidths in ZnO-based systems can reflect overlapping contributions and relaxation effects, ESR is interpreted here as complementary evidence for defect-related paramagnetic centers, without assigning a unique microscopic origin solely based on g-values.

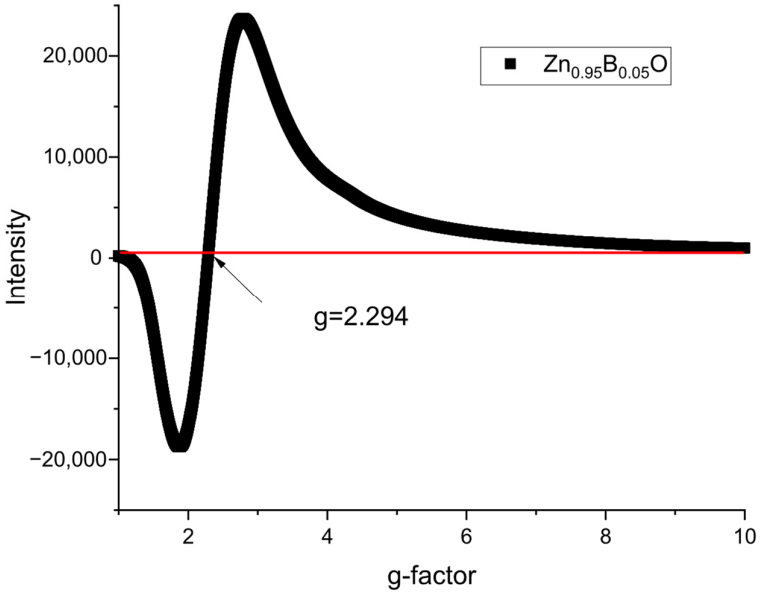

Figure 13. The g-factors were calculated from the ESR spectra of the ZnO: 5%B NPs.

Consistently, the defect chemistry inferred from PL is dominated by zinc interstitials (Zn_i) and zinc vacancies (V_{Zn}) with contributions from oxygen-related centers (O_i) is qualitatively consistent with the presence of a strong ESR signal arising from a defect-rich paramagnetic environment. The fact that $P_{asy} > 1$ and the large ΔH_{pp} further suggest magnetic microstructural heterogeneity between surface and core regions and multiple relaxation channels in the nanoparticles, in line with the relatively high population of unpaired spins (N_s). Here, N_s is reported as a relative estimate based on the adopted analysis expression and experimental conditions, and it is used for qualitative/within-study comparison rather than as an absolute calibrated spin concentration

Overall, ESR confirms a defect-rich and locally strained/disordered magnetic environment associated with paramagnetic defect centers induced by B incorporation, which, together with the PL violet/blue bands, support a scenario wherein $B^{3+} \rightarrow Zn^{2+}$ substitution drives charge-compensation and size-mismatch mechanisms as the primary sources of defects, as shown in Figure 11 and Table 11.

3. Materials and Methods

3.1. Experimental Procedure

ZnO: 5%B nanoparticles were synthesized via a sol–gel route using zinc acetate dihydrate ($Zn(CH_3COO)_2 \cdot 2H_2O$) and boric acid ($H_3BO_3$) as the zinc and boron sources, respectively. Methanol (CH_3OH) was employed as the solvent to ensure homogeneous precursor dispersion, while monoethanolamine (MEA, C_2H_7NO) acted as a chelating and stabilizing agent.

Stoichiometric amounts of each precursor were accurately weighed using an analytical balance to prepare 0.25 M solutions in 100 mL beakers containing Teflon-coated magnetic stir bars. The precursor solutions were mixed with 80 mL of methanol and 1500 µL of MEA, sealed with Parafilm to prevent premature solvent loss, and magnetically stirred at 300 rpm for 24 h under ambient conditions. After stirring was completed, the Parafilm was removed to allow controlled solvent evaporation, resulting in the formation of a viscous gel. The magnetic stir bars were removed prior to heat treatment to prevent extraneous contamination.

Thermal processing of the dried gels was carried out in a furnace following a two-step calcination protocol. The samples were first heated to 400 °C for 10 min to decompose

residual organic species, and subsequently annealed at 600 °C for 30 min to promote crystallization of the ZnO: 5%B nanoparticles. The resulting powders were ground to achieve a uniform particle-size distribution.

3.2. Structural Analysis

X-ray diffraction (XRD; Rigaku (Tokyo, Japan), Cu Kα) was used to characterize the sample's structure. Scanning electron microscopy (SEM; JEOL JSM-5910LV (Tokyo, Japan)) was employed to characterize the surface morphology, and photoluminescence (PL) spectroscopy (Agilent Cary Eclipse (Santa Clara, CA, USA)) was used to evaluate its optical characteristics. With conventional conditions (5 mW power, 0.03 s time constant), magnetic characterization was accomplished using electron spin resonance (ESR) spectroscopy on a Jeol JES-FA300 (Tokyo, Japan) spectrometer running at 9.45 GHz with a TE_{102} cavity. A static magnetic field range of 0–1000 mT was used to record ESR spectra. The background signal of the resonant cavity and the empty quartz sample tubes was subtracted from the data to increase accuracy.

4. Conclusions

In this study, ZnO: 5% B nanoparticles synthesized via the sol–gel method exhibited a single-phase wurtzite structure, and their crystal integrity was confirmed by XRD. Analysis of line broadening revealed that the average crystallite size was in the range of 32.37–39.63 nm, while the microstrain was on the order of 2×10^{-4}. Moreover, the positive slopes in the Williamson–Hall plots indicated that tensile stresses were dominant. Optical measurements using the Kubelka–Munk/Tauc approach yielded a band gap of $E_g = 3.216$ eV, which represents a slight narrowing compared to pure ZnO. This result supports the conclusion that $B^{3+} \rightarrow Zn^{2+}$ substitution increases the density of edge states and enhances the band-tailing effect. Indeed, the Urbach energy ($E_u =$ 184–193 meV) is consistent with short-range bond distortions and localization effects.

Refractive index values calculated from five different $n(E_g)$ models ranged between 2.05 and 2.71, confirming the material's potential for optoelectronic applications within the wide band gap/high refractive index window.

Gaussian deconvolution of the PL spectrum revealed that the violet (Zn_i) and blue (V_{Zn}) bands were dominant, while the red (O_i) contribution was relatively limited. This defect chemistry indicates an enrichment of zinc vacancy/interstitial centers as an inevitable consequence of charge compensation and size mismatch. ESR measurements exhibited a single, broad, and intense resonance line ($g = 2.294$, $\Delta H_{pp} \approx 120.7$ mT), suggesting the predominance of paramagnetic defect centers and a high defect density.

Because B doping in ZnO efficiently affects the crystal–chemical defect landscape while subtly changing band-edge states and optical constants, it has potential use in transparent conducting films, electron transport layers in organic photovoltaics (OPVs), and UV photo detection.

Author Contributions: Conceptualization, L.A. and E.O.; methodology, L.A.; formal analysis, L.A. and E.O.; investigation, I.T. and M.M.S.P.; data curation, L.A.; writing—original draft preparation, L.A.; writing—review and editing, E.O. and I.T.; visualization, L.A.; supervision, L.A. and E.O. All authors have read and agreed to the published version of the manuscript.

Funding: This research was supported by the Research Fund of Bahcesehir University (BAU-BAP.2018.02.16).

Institutional Review Board Statement: Not applicable.

Informed Consent Statement: Not applicable.

Data Availability Statement: The original contributions presented in this study are included in the article. Further inquiries can be directed to the corresponding author.

Conflicts of Interest: The authors have no conflicts of interest to declare that are relevant to the content of this article.

References

1. Bagnall, D.M.; Chen, Y.F.; Zhu, Z.; Yao, T.; Koyama, S.; Shen, M.Y.; Goto, T. Optically pumped lasing of ZnO at room temperature. *Appl. Phys. Lett.* **1997**, *70*, 2230–2232. [CrossRef]
2. Shionoya, S.; Yen, W.M.; Yamamoto, H. (Eds.) *Phosphor Handbook*; CRC Press: Boca Raton, FL, USA, 2018.
3. Janotti, A.; Van de Walle, C.G. Fundamentals of zinc oxide as a semiconductor. *Rep. Prog. Phys.* **2009**, *72*, 126501. [CrossRef]
4. Pathak, T.K.; Kumar, V.; Prakash, J.; Purohit, L.P.; Swart, H.C.; Kroon, R.E. Fabrication and characterization of nitrogen-doped p-ZnO on n-Si heterojunctions. *Sens. Actuators A Phys.* **2016**, *247*, 475–481. [CrossRef]
5. Hauffe, K.; Vierk, A.L. Über die elektrische Leitfähigkeit von Zinkoxyd mit Fremdoxydzusätzen. *Z. Für Phys. Chem.* **1950**, *196*, 160–180. [CrossRef]
6. Ling, C.; Guo, T.; Shan, M.; Zhao, L.; Sui, H.; Ma, S.; Xue, Q. Oxygen vacancies enhanced photoresponsive performance of ZnO nanoparticles thin film/Si heterojunctions for ultraviolet/infrared photodetector. *J. Alloys Compd.* **2019**, *797*, 1224–1231. [CrossRef]
7. Khan, M.A.; Singha, M.K.; Nanda, K.K.; Krupanidhi, S.B. Defect and strain modulated highly efficient ZnO UV detector: Temperature and low-pressure dependent studies. *Appl. Surf. Sci.* **2020**, *505*, 144365. [CrossRef]
8. Shi, X.; Wu, L.; Hong, P.; Teng, F.; Hu, P.; Fan, H. A review of recent advances in ZnO-based thin film photodetectors: Preparation, structure and strategies for performance enhancement. *Opt. Laser Technol.* **2025**, *191*, 113352. [CrossRef]
9. Han, X.-G.; Jiang, Y.-Q.; Xie, S.-F.; Kuang, Q.; Zhou, X.; Cai, D.-P.; Xie, Z.-X.; Zheng, L.-S. Control of the surface of ZnO nanostructures by selective wet-chemical etching. *J. Phys. Chem. C* **2010**, *114*, 10114–10118. [CrossRef]
10. Nam, T.; Zywotko, D.R.; Colleran, T.A.; Partridge, J.L.; George, S.M. Thermal Atomic Layer Etching of Zinc Oxide from 30–300 °C Using Sequential Exposures of Hydrogen Fluoride and Trimethylgallium. *Chem. Mater.* **2025**, *37*, 2844–2854. [CrossRef]
11. Naccarato, F.; Ricci, F.; Suntivich, J.; Hautier, G.; Wirtz, L.; Rignanese, G.-M. Searching for materials with high refractive index and wide band gap: A first-principles high-throughput study. *Phys. Rev. Mater.* **2019**, *3*, 044602. [CrossRef]
12. Arda, L.; Raad, Z.; Veziroglu, S.; Tav, C.; Yahsi, U. The Influence of Defects on the Structural, Optical, and Antibacterial Properties of Cr/Cu Co-Doped ZnO Nanoparticles. *J. Mol. Struct.* **2025**, *1320*, 139663. [CrossRef]
13. Bose, S.; Mandal, S.; Barua, A.K.; Mukhopadhyay, S. Properties of boron doped ZnO films prepared by reactive sputtering method: Application to amorphous silicon thin film solar cells. *J. Mater. Sci. Technol.* **2020**, *55*, 136–143. [CrossRef]
14. Shankar, P.; Srinivasan, P.; Vutukuri, B.; Kulandaisamy, A.J.; Mani, G.K.; Babu, K.J.; Lee, J.H.; Rayappan, J.B.B. Boron induced c-axis growth and ammonia sensing signatures of spray pyrolysis deposited ZnO thin films: Relation between crystallinity and sensing. *Thin Solid Film.* **2022**, *746*, 139126. [CrossRef]
15. Alsaad, M.; Al-Bataineh, Q.M.; Ahmad, A.A.; Albataineh, Z.; Telfah, A. Optical band gap and refractive index dispersion parameters of boron-doped ZnO thin films: A novel derived mathematical model from the experimental transmission spectra. *Optik* **2020**, *211*, 164641. [CrossRef]
16. Atılgan, A.; Özel, K. Boron-doped thin films fabricated by the spin coating method: The effect of doping concentrations. *Gazi Univ. J. Sci. Part A Eng. Innov.* **2024**, *11*, 57–67. [CrossRef]
17. Kumar, V.; Singh, R.; Purohit, L.; Mehra, R. Structural, Transport, and Optical Properties of Boron-Doped Zinc Oxide Nanocrystalline. *J. Mater. Sci. Technol.* **2011**, *27*, 481–488. [CrossRef]
18. Muthukumaran, S.; Gopalakrishnan, R. Structural, FTIR, and photoluminescence studies of Cu doped ZnO nanopowders by the co-precipitation method. *Opt. Mater.* **2012**, *34*, 1946–1953. [CrossRef]
19. Arda, L.; Karatas, O.; Alphan, M.C.; Ozugurlu, E. Electron spin resonance and photoluminescence studies of Co/Mg co-doped ZnO nanoparticles. *Int. J. Appl. Ceram. Technol.* **2024**, *21*, 2458–2473. [CrossRef]
20. Xu, X.G.; Yang, H.L.; Wu, Y.; Zhang, D.L.; Wu, S.Z.; Miao, J.; Jiang, Y.; Qin, X.B.; Cao, X.Z.; Wang, B.Y. Intrinsic room temperature ferromagnetism in boron-doped ZnO. *Appl. Phys. Lett.* **2010**, *97*, 232502. [CrossRef]
21. Ristić, M.; Musić, S.; Ivanda, M.; Popović, S. Sol–gel synthesis and characterization of nanocrystalline ZnO powders. *J. Alloys Compd.* **2005**, *397*, L1–L4. [CrossRef]
22. Arda, L. The effects of Tb-doped ZnO nanorod: An EPR study. *J. Magn. Magn. Mater.* **2019**, *475*, 493–501. [CrossRef]
23. Kumar, R.; Hymavathi, B. X-ray peak profile analysis of solid-state sintered alumina-doped zinc oxide ceramics by Williamson–Hall and size-strain plot methods. *J. Asian Ceram. Soc.* **2017**, *5*, 94–103. [CrossRef]
24. Stokes, R.; Wilson, A.J.C. The diffraction of X-rays by distorted crystal aggregates—I. *Proc. Phys. Soc.* **1944**, *56*, 174–181. [CrossRef]
25. Mote, V.D.; Dargad, J.S.; Purushotham, Y.; Dole, B.N. Effect of doping on structural, physical, morphological, and optical properties of Zn1−xMnxO nanoparticles. *Ceram. Int.* **2015**, *41*, 15153–15161. [CrossRef]

26. Perdew, J.P.; Burke, K.; Ernzerhof, M. Generalized gradient approximation made simple. *Phys. Rev. Lett.* **1996**, *77*, 3865–3868. [CrossRef]
27. Boukhvalov, W.; Lichtenstein, A.I.; Dobrovitski, V.V.; Katsnelson, M.I.; Harmon, B.N.; Mazurenko, V.V.; Anisimov, V.I. Effect of local Coulomb interactions on the electronic structure and exchange interactions in Mn12 magnetic molecules. *Phys. Rev. B* **2002**, *65*, 184435. [CrossRef]
28. Mahendiran, M.; Mathen, J.J.; Racik, M.; Madhavan, J.; Raj, M.V.A. Investigation of structural, optical, and electrical properties of transition metal oxide semiconductor CdOZnO nanocomposite and its effective role in the removal of water contaminants. *J. Phys. Chem. Solids* **2019**, *126*, 322–334. [CrossRef]
29. Ravindra, N.M.; Auluck, S.; Srivastava, V.K. On the Penn Gap in Semiconductors. *Phys. Status Solidi B* **1979**, *93*, K155–K160. [CrossRef]
30. Moss, T.S. Relations between the refractive index and energy gap of semiconductors. *Phys. Status Solidi B* **1985**, *131*, 415–427. [CrossRef]
31. Hervé, P.; Vandamme, L. General relation between refractive index and energy gap in semiconductors. *Infrared Phys. Technol.* **1994**, *35*, 609–615. [CrossRef]
32. Reddy, R.R.; Anjaneyulu, S. Analysis of the Moss and Ravindra relations. *Phys. Status Solidi B* **1992**, *174*, K91–K93. [CrossRef]
33. Kumar, V.; Singh, J. Model for calculating the refractive index of different materials. *Indian J. Pure Appl. Phys.* **2010**, *48*, 571–574.
34. Tripathy, S. Refractive Indices of Semiconductors from Energy gaps. *Opt. Mater.* **2015**, *46*, 240–246. [CrossRef]
35. He, H.; Zhuge, F.; Ye, Z.; Zhu, L.; Wang, F.; Zhao, B.; Huang, J. Strain and its effect on optical properties of Al-N codoped ZnO films. *J. Appl. Phys.* **2006**, *99*, 023503. [CrossRef]
36. Vettumperumal, R.; Kalyanaraman, S.; Santoshkumar, B.; Thangavel, R. Estimation of electron-phonon coupling and Urbach energy in group-I elements doped ZnO nanoparticles and thin films by sol-gel method. *Mater. Res. Bull.* **2016**, *77*, 101–110. [CrossRef]
37. Bindu, P.; Thomas, S. Optical properties of ZnO nanoparticles synthesized from a polysaccharide and $ZnCl_2$. *Acta Phys. Pol. A* **2017**, *131*, 1474–1478. [CrossRef]
38. Kamitsos, E.I.; Patsis, A.P.; Karakassides, M.A.; Chryssikos, G.D. Infrared reflectance spectra of lithium borate glasses. *J. Non-Cryst. Solids* **1990**, *126*, 52–67. [CrossRef]
39. Pascuta, P.; Lungu, R.; Ardelean, I. FTIR and Raman spectroscopic investigation of some strontium–borate glasses doped with iron ions. *J. Mater. Sci. Mater. Electron.* **2010**, *21*, 548–553. [CrossRef]
40. Brik, M.G.; Srivastava, A.M.; Popov, A.I. A few common misconceptions in the interpretation of experimental spectroscopic data. *Opt. Mater.* **2022**, *127*, 112276. [CrossRef]
41. Uklein, V.; Multian, V.V.; Kuz, G.M.; Linnik, R.P.; Lisnyak, V.V.; Popov, A.I.; Gayvoronsky, V.Y. Nonlinear optical response of bulk ZnO crystals with different content of intrinsic defects. *Opt. Mater.* **2018**, *84*, 738–747. [CrossRef]